Structures 75 (2025) 108673

Contents lists available at ScienceDirect

Structures

journal homepage: www.elsevier.com/locate/structures

Efficient generation of standard and non-standard influence functions using Generalized Beam Theory

David Henriques [a], Nuno Peres [b], Rodrigo Gonçalves [c,*]

[a] PPE Structural Engineering, R. Jaime Batalha Reis 1C, 1500-679 Lisbon, and Departamento de Engenharia Civil, Faculdade de Ciências e Tecnologia, Universidade NOVA de Lisboa, 2829-516 Caparica, Portugal
[b] CERIS and Faculty of Engineering, Universidade Lusófona, 1749-024 Lisbon, Portugal
[c] CERIS and Departamento de Engenharia Civil, Faculdade de Ciências e Tecnologia, Universidade NOVA de Lisboa, 2829-516 Caparica, Portugal

ARTICLE INFO

Keywords:
Influence surfaces
Influence lines
Thin-walled structures
Cross-section deformation
Generalized Beam Theory

ABSTRACT

In structural analysis and design, influence functions (lines and surfaces) are extremely valuable for identifying the most unfavorable positions of live loads. This paper introduces a computationally efficient method for calculating non-standard influence functions using Generalized Beam Theory (GBT), a thin-walled beam theory that allows cross-section deformation by means of hierarchical and structurally meaningful "cross-section deformation modes". Consequently, the proposed method enables not only the calculation standard influence functions (for displacements, support reactions and stress resultants), but also those pertaining to higher-order cross-section deformation (torsion, distortion, plate bending, etc.), their strains, stress resultants and mode amplitudes. The computational cost of the procedure is equivalent to that of a single linear analysis of the structure and its implementation is straightforward. Several illustrative examples are presented to show the capabilities of the proposed method.

1. Introduction

The design of structures requires assessing its response under different load cases and combinations, ensuring that the most unfavorable positions of live loads are accounted for. The latter requirement motivates the use of influence functions (lines or surfaces, depending on the load path), which provide the value of a given effect — typically displacements, support reactions and stress resultants — in terms of the position of a unit moving load.

Performing a structural analysis for each possible position of the load is not effective and therefore indirect methods are used instead, which essentially stem from the reciprocity theorems of Betti and Maxwell. For frames, influence lines for stress resultants and reactions are commonly calculated using the well known Müller-Breslau principle, whereby a release is introduced and a relative unit displacement is imposed, so that the influence line corresponds to the deflected shape of the structure. A thorough account of the early methods for the calculation of influence surfaces can be found in [1,2].

The subsequent fast development of the Finite Element Method has introduced the means to automate the calculation of influence functions. For displacements, it is straightforward to apply the indirect method to a finite element model, while for other effects either the Müller-Breslau principle is used (see e.g. [3]), which requires the introduction of a release in the model, or equivalent forces are applied to the original model. Fu [4] obtained influence surfaces for stress resultants in plates by applying equivalent nodal forces that approximately reproduce the unit displacement effect of the Müller-Breslau principle. For 2D frames, Belegundu [5] followed an analogy with the standard optimization problem of calculating the sensitivity (the influence line) of an objective function (the sought effect) with respect to certain design variables (the loads), designating it the "adjoint method". Corrections for discontinuities and reactions were discussed in [6]. The adjoint method corresponds to the application of equivalent (and consistent) nodal forces to the model, but the analogy with the optimization problem is not essential. In fact, a simpler derivation is possible, as shown in Section 3.2. This simpler approach was apparently first proposed by Okradogen and Girgin [7], in the case of both influence lines and surfaces. For 2D Euler–Bernoulli beams, expressions for the equivalent nodal forces and the corrections for discontinuities are provided in [8].

The Generalized Beam Theory (GBT) is a thin-walled beam theory known for its ability to capture global–local–distortional deformation with remarkable accuracy and computational efficiency. GBT was originally proposed by Schardt [9,10] and has been continuously developed, see e.g. the bibliography listed in [11], at http://vtb.info/ and at

* Corresponding author.
E-mail address: rodrigo.goncalves@fct.unl.pt (R. Gonçalves).

https://doi.org/10.1016/j.istruc.2025.108673
Received 4 December 2024; Received in revised form 5 February 2025; Accepted 11 March 2025
Available online 22 March 2025

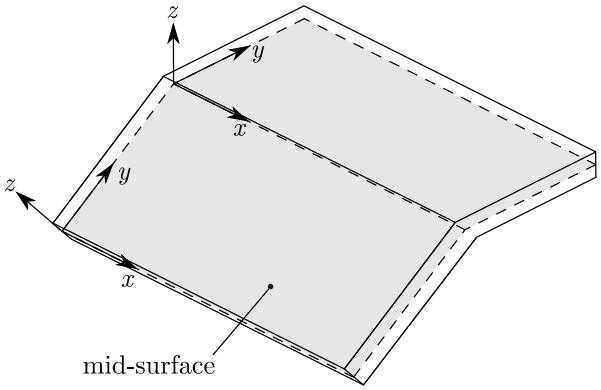

Fig. 1. GBT wall local axes (x, y, z), where x defines the longitudinal direction of the beam.

https://sites.fct.unl.pt/gbt/ In GBT, the beam configuration is expressed in terms of a hierarchical set of so-called "cross-section deformation modes", which constitute an extension of the Vlasov thin-walled beam theory. Consequently, the solution is expressed in terms of the amplitudes of each mode, a feature that conveys a unique insight into the mechanics of the problem. It should be emphasized that using only the so-called "conventional" (the first few) deformation modes generally leads to quite accurate results in a wide range of cases.

This paper proposes a computationally efficient GBT-based method for the calculation of influence functions (lines and surfaces) for thin-walled members susceptible to cross-section deformation. The use of GBT allows obtaining not only standard influence functions (displacements, support reactions and stress resultants), but also non-standard ones, pertaining to higher-order cross-section deformation and their corresponding stress resultants. The method is based on the equivalent nodal force concept and therefore the computational cost is equivalent to that of a single linear analysis of the member.

The outline of the paper is as follows. Section 2 presents a brief overview of the linear GBT, to introduce the fundamental equations and a standard displacement-based finite element. Section 3 presents the proposed approach for the calculation of influence functions. The approach allows several effects — displacements, rotations, strains, stresses, stress resultants, mode amplitudes and support reactions — and moving load types — forces, moments and generalized section-wise forces. Several numerical examples are presented in Section 4, to illustrate the capabilities of the proposed method. The paper closes in Section 5, with the concluding remarks.

The GBT vector-matrix notation introduced in [12] is followed, where bold letters are used for vectors (column vectors except where stated otherwise) and matrices. Derivatives are generally indicated by subscript commas (e.g. $f(y)_{,y} = \mathrm{d}f/\mathrm{d}y$), with the prime used for derivatives with respect to x. In addition, $\boldsymbol{e}_k$ is a (column) vector with its kth entry equal to 1 (the kth vector of the canonical basis of $\mathbb{R}^n$).

2. Overview of the linear GBT

2.1. Displacements and strain

The mid-surface displacements of each wall (u, v, w), defined along the wall local axes $(x, y, z$ resp.), see Fig. 1, are expressed as sum of $k = 1, \ldots, D$ known deformation modes, see [13–15], with mid-surface components $\bar{u}_k(y)$, $\bar{v}_k(y)$, $\bar{w}_k(y)$, each one multiplied by its amplitude function $\phi_k(x)$, viz.

$$u(x,y) = \sum_{k=1}^{D} \bar{u}_k(y)\ \phi'_k(x) = \bar{\boldsymbol{u}}^T \boldsymbol{\phi}', \tag{1}$$

$$v(x,y) = \sum_{k=1}^{D} \bar{v}_k(y)\ \phi_k(x) = \bar{\boldsymbol{v}}^T \boldsymbol{\phi}, \tag{2}$$

$$w(x,y) = \sum_{k=1}^{D} \bar{w}_k(y)\ \phi_k(x) = \bar{\boldsymbol{w}}^T \boldsymbol{\phi}, \tag{3}$$

where the vectors on the right hand side collect the corresponding components. It is worth recalling that ϕ'_k (the derivative of ϕ_k with respect to x) must be used in Eq. (1) to allow using Vlasov's null membrane shear strain assumption when needed. For future convenience, the amplitude function vectors are grouped in vector $\boldsymbol{\Phi}$ according to

$$\boldsymbol{\Phi}(x) = \begin{bmatrix} \boldsymbol{\phi} \\ \boldsymbol{\phi}' \\ \boldsymbol{\phi}'' \end{bmatrix}. \tag{4}$$

The displacement vector for each wall, $\boldsymbol{U}$, can be expressed in terms of u, v, w using Kirchhoff's thin plate assumption, leading to

$$\boldsymbol{U} = \boldsymbol{\Xi}_U(y,z)\boldsymbol{\Phi}(x), \tag{5}$$

$$\boldsymbol{\Xi}_U = \begin{bmatrix} \boldsymbol{0} & \bar{\boldsymbol{u}}^T - z\bar{\boldsymbol{w}}^T & \boldsymbol{0} \\ \bar{\boldsymbol{v}}^T - z\bar{\boldsymbol{w}}'^T & \boldsymbol{0} & \boldsymbol{0} \\ \bar{\boldsymbol{w}}^T & \boldsymbol{0} & \boldsymbol{0} \end{bmatrix}. \tag{6}$$

This leads to the strain–displacement relations

$$\boldsymbol{\varepsilon} = \begin{bmatrix} \varepsilon_{xx} \\ \varepsilon_{yy} \\ \gamma_{xy} \end{bmatrix} = \boldsymbol{\Xi}_\varepsilon(y,z)\boldsymbol{\Phi}(x), \tag{7}$$

$$\boldsymbol{\Xi}_\varepsilon = \begin{bmatrix} \boldsymbol{0} & \boldsymbol{0} & \bar{\boldsymbol{u}}^T - z\bar{\boldsymbol{w}}'^T \\ \bar{\boldsymbol{v}}'^T - z\bar{\boldsymbol{w}}''^T & \boldsymbol{0} & \boldsymbol{0} \\ \boldsymbol{0} & (\bar{\boldsymbol{u}}' + \bar{\boldsymbol{v}})^T - 2z\bar{\boldsymbol{w}}'^T & \boldsymbol{0} \end{bmatrix}. \tag{8}$$

2.2. Stresses and stress resultants

Assuming a plane stress state and a linear elastic isotropic material, the stresses are obtained using

$$\boldsymbol{\sigma} = \begin{bmatrix} \sigma_{xx} \\ \sigma_{yy} \\ \sigma_{xy} \end{bmatrix} = \boldsymbol{\Xi}_\sigma(y,z)\boldsymbol{\Phi}(x), \tag{9}$$

$$\boldsymbol{\Xi}_\sigma = \boldsymbol{C}\boldsymbol{\Xi}_\varepsilon, \tag{10}$$

$$\boldsymbol{C} = \begin{bmatrix} \frac{E}{1-\nu^2} & \frac{\nu E}{1-\nu^2} & 0 \\ \frac{\nu E}{1-\nu^2} & \frac{E}{1-\nu^2} & 0 \\ 0 & 0 & G \end{bmatrix}, \tag{11}$$

with Young's modulus E, Poisson's ratio ν and the shear modulus G. If $\varepsilon^M_{yy} = 0$ is assumed, which is acceptable in a wide range of cases, one uses instead for the membrane terms

$$\boldsymbol{C} = \begin{bmatrix} E & 0 & 0 \\ 0 & 0 & 0 \\ 0 & 0 & G \end{bmatrix}, \tag{12}$$

otherwise over-stiff solutions are obtained due to restrained Poisson effects (the null diagonal entry is irrelevant since $\varepsilon^M_{yy} = 0$).

The stress resultants are given by

$$\boldsymbol{\mathcal{X}}_{xx} = \int_A \left(\boldsymbol{\Xi}^{(1,3)}_\varepsilon\right)^T \sigma_{xx}\ \mathrm{d}A, \tag{13}$$

$$\boldsymbol{\mathcal{X}}_{yy} = \int_A \left(\boldsymbol{\Xi}^{(2,1)}_\varepsilon\right)^T \sigma_{yy}\ \mathrm{d}A, \tag{14}$$

$$\boldsymbol{\mathcal{X}}_{xy} = \int_A \left(\boldsymbol{\Xi}^{(3,2)}_\varepsilon\right)^T \sigma_{xy}\ \mathrm{d}A, \tag{15}$$

where the components of $\boldsymbol{\mathcal{X}}_{xx}$ correspond to axial force, bending moments, bimoment and higher-order bimoments, the components of $\boldsymbol{\mathcal{X}}_{yy}$ are associated with transverse normal stresses and the components of $\boldsymbol{\mathcal{X}}_{xy}$ are shear stress resultants. These resultants can be written as

$$\boldsymbol{\mathcal{X}} = \begin{bmatrix} \boldsymbol{\mathcal{X}}_{yy} \\ \boldsymbol{\mathcal{X}}_{xy} \\ \boldsymbol{\mathcal{X}}_{xx} \end{bmatrix} = \boldsymbol{\mathcal{M}}\boldsymbol{\Phi}(x), \tag{16}$$

$$\mathcal{M} = \begin{bmatrix} \mathbf{B} & \mathbf{0} & \mathbf{D}_2 \\ \mathbf{0} & \mathbf{D}_1 & \mathbf{0} \\ \mathbf{D}_2^T & \mathbf{0} & \mathbf{C} \end{bmatrix}, \tag{17}$$

where $\mathbf{B}$, $\mathbf{C}$, $\mathbf{D}_1$ and $\mathbf{D}_2$ are the so-called GBT modal matrices, which are obtained from the cross-section integration of the deformation modes,

$$\mathbf{B} = \int_S \frac{E}{1-\nu^2} \left(t\bar{\boldsymbol{v}}_{,y}\bar{\boldsymbol{v}}_{,y}^T + \frac{t^3}{12}\bar{\boldsymbol{w}}_{,yy}\bar{\boldsymbol{w}}_{,yy}^T \right) \mathrm{d}y, \tag{18}$$

$$\mathbf{C} = \int_S \left(\frac{Et}{1-\nu^2}\bar{\boldsymbol{u}}\bar{\boldsymbol{u}}^T + \frac{Et^3}{12(1-\nu^2)}\bar{\boldsymbol{w}}\bar{\boldsymbol{w}}^T \right) \mathrm{d}y, \tag{19}$$

$$\mathbf{D}_1 = \int_S G \left(t(\bar{\boldsymbol{u}}_{,y} + \bar{\boldsymbol{v}})(\bar{\boldsymbol{u}}_{,y} + \bar{\boldsymbol{v}})^T + \frac{t^3}{3}\bar{\boldsymbol{w}}_{,y}\bar{\boldsymbol{w}}_{,y}^T \right) \mathrm{d}y, \tag{20}$$

$$\mathbf{D}_2 = \int_S \frac{\nu E}{1-\nu^2} \left(t\bar{\boldsymbol{v}}_{,y}\bar{\boldsymbol{u}}^T + \frac{t^3}{12}\bar{\boldsymbol{w}}_{,yy}\bar{\boldsymbol{w}}^T \right) \mathrm{d}y. \tag{21}$$

If $\varepsilon_{yy}^M = 0$, the term $Et/(1-\nu^2)$ in $\mathbf{C}$ is replaced by Et.

The homogeneous differential equilibrium equations read, in terms of stress resultants,

$$\boldsymbol{\mathcal{X}}_{xx}'' + \boldsymbol{\mathcal{X}}_{yy} - \boldsymbol{\mathcal{X}}_{xy}' = \mathbf{0} \tag{22}$$

or, in terms of GBT modal matrices,

$$\mathbf{C}\boldsymbol{\phi}'''' - \mathbf{D}\boldsymbol{\phi}'' + \mathbf{B}\boldsymbol{\phi} = \mathbf{0}, \tag{23}$$

with $\mathbf{D} = \mathbf{D}_1 - \mathbf{D}_2 - \mathbf{D}_2^T$.

2.3. The standard displacement-based finite element

The linear version of the beam finite element proposed in [12,16] is used in this work. The interpolation functions correspond to Hermite cubic and Lagrange quadratic polynomials, the latter used only for the deformation modes that only involve warping displacements (e.g. the axial extension mode). The interpolation is of the form

$$\boldsymbol{\phi} = \boldsymbol{\psi}\boldsymbol{d}_e, \tag{24}$$

where matrix $\boldsymbol{\psi}$ contains the interpolation functions and vector $\boldsymbol{d}_e$ collects their nodal values, the finite element DOFs.

The element stiffness matrix is given by

$$\boldsymbol{K}_e = \int_{L_e} \boldsymbol{\Psi}^T \boldsymbol{\mathcal{M}} \boldsymbol{\Psi} \, \mathrm{d}x, \tag{25}$$

$$\boldsymbol{\Psi} = \begin{bmatrix} \boldsymbol{\psi} \\ \boldsymbol{\psi}' \\ \boldsymbol{\psi}'' \end{bmatrix}, \tag{26}$$

where L_e is the finite element length. For body forces $\boldsymbol{q}$, the element load vector is given by

$$\boldsymbol{F}_e = \int_V \boldsymbol{\Psi}^T \boldsymbol{\Xi}_U^T \boldsymbol{q} \, \mathrm{d}V. \tag{27}$$

The assembly of the element matrices and vectors then yields the standard equation

$$\boldsymbol{K}\boldsymbol{d} = \boldsymbol{F}. \tag{28}$$

3. GBT-based influence surfaces

3.1. DOF selection and projection

Let subscripts u and r designate the unrestrained and restrained nodal DOFs of the GBT-based finite element model. The finite element solution requires solving

$$\boldsymbol{K}_u\boldsymbol{d}_u = \boldsymbol{F}_u. \tag{29}$$

These "u versions" of the matrix/vectors in Eq. (28) can be efficiently obtained using index-based selection techniques in programming. However, for the following developments, which require algebraic manipulation, it is useful to define the *selection* matrix $\boldsymbol{\mathcal{S}}_u$ such that

$$\boldsymbol{d}_u = \boldsymbol{\mathcal{S}}_u\boldsymbol{d}. \tag{30}$$

Each row of this matrix is of the form of $\boldsymbol{e}_k^T$, with k spanning the unrestrained DOF space only. Its transpose defines the *projection* matrix $\boldsymbol{\mathcal{P}}_u = \boldsymbol{\mathcal{S}}_u^T$, which in this case defines the inverse operation,

$$\boldsymbol{d} = \boldsymbol{\mathcal{P}}_u\boldsymbol{d}_u, \tag{31}$$

since the restrained displacements are null ($\boldsymbol{d}_r = \mathbf{0}$).

Let the selection matrix $\boldsymbol{\mathcal{S}}_e^m$ (also a matrix with rows in the form of $\boldsymbol{e}_k^T$) collect $\boldsymbol{d}_e^m$ — pertaining to the mth finite element — from $\boldsymbol{d}$, using

$$\boldsymbol{d}_e^m = \boldsymbol{\mathcal{S}}_e^m\boldsymbol{d} = \boldsymbol{\mathcal{S}}_e^m\boldsymbol{\mathcal{P}}_u\boldsymbol{d}_u = \boldsymbol{\mathcal{S}}_{eu}^m\boldsymbol{d}_u, \tag{32}$$

where $\boldsymbol{\mathcal{S}}_{eu}^m = \boldsymbol{\mathcal{S}}_e^m\boldsymbol{\mathcal{P}}_u$ can be viewed as a selection matrix since the missing displacements in $\boldsymbol{d}_u$ (the restrained DOFs) are null. Its transpose $\left(\boldsymbol{\mathcal{S}}_{eu}^m\right)^T = \boldsymbol{\mathcal{P}}_{eu}^m$ projects the components of $\boldsymbol{d}_e^m$ to their positions to a vector in the unrestrained DOF space, defining vector $\boldsymbol{d}_u^m$,

$$\boldsymbol{d}_u^m = \boldsymbol{\mathcal{P}}_{eu}^m\boldsymbol{d}_e^m. \tag{33}$$

3.2. Calculation of influence surfaces

Let f designate the sought effect, calculated at the nth finite element — the *target* element. The effect can be obtained from the element DOFs through a relation of the type

$$f = \boldsymbol{T}_f\boldsymbol{d}_e^n, \tag{34}$$

where $\boldsymbol{T}_f$ is a row vector that depends on the nature of the effect (see Section 3.3). Using the previous relations, it is possible to write

$$f = \underbrace{\boldsymbol{T}_f\boldsymbol{\mathcal{S}}_{eu}^n\boldsymbol{K}_u^{-1}}_{\boldsymbol{f}_u^T}\boldsymbol{F}_u. \tag{35}$$

where $\boldsymbol{f}_u$ is a vector. It should be noted that

Remark 3.1. the kth element of vector $\boldsymbol{f}_u$ is the effect f when $\boldsymbol{F}_u = \boldsymbol{e}_k$, i.e., when a unit load, work-conjugate to the kth DOF, is applied.

By simple algebraic manipulation, the problem of calculating the effect for several positions of the load (several $\boldsymbol{F}_u$) is transformed to the calculation of a single vector, $\boldsymbol{f}_u$. Except for reactions (see Section 3.3), the complete vector can be obtained with $\boldsymbol{f} = \boldsymbol{\mathcal{P}}_u\boldsymbol{f}_u$ since $\boldsymbol{f}_r = \mathbf{0}$, in other words, since the effect is null when the unit load is work-conjugate to a restrained DOF.

Eq. (35) provides an expression for the evaluation of $\boldsymbol{f}_u$,

$$\boldsymbol{K}_u\boldsymbol{f}_u = \boldsymbol{\mathcal{P}}_{eu}^n\boldsymbol{T}_f^T. \tag{36}$$

To achieve this format, which is analogous to that of Eq. (29), advantage was taken from the symmetry of the stiffness matrix (actually of its inverse). Consequently, $\boldsymbol{f}_u$ is the "displacement" when the "load" is $\boldsymbol{\mathcal{P}}_{eu}^n\boldsymbol{T}_f^T$, the projection of the "element load" $\boldsymbol{T}_f^T$ to the unrestrained DOF space. In other words, recalling Remark 3.1,

Remark 3.2. the kth element of $\boldsymbol{f}_u$ (the sought effect when $\boldsymbol{F}_u = \boldsymbol{e}_k$) is also the kth displacement when $\boldsymbol{F}_u = \boldsymbol{\mathcal{P}}_{eu}^n\boldsymbol{T}_f^T$.

This constitutes a generalization of Betti's reciprocal work theorem, as discussed in Section 3.5.

For further developments, let f^m designate the effect when the load is in element m. This effect can be calculated from the subvectors of the vectors in Eq. (35) pertaining to that element,

$$f^m = \underbrace{\left(\boldsymbol{\mathcal{S}}_{eu}^m\boldsymbol{f}_u\right)^T}_{\left(\boldsymbol{f}_e^m\right)^T}\underbrace{\boldsymbol{\mathcal{S}}_{eu}^m\boldsymbol{F}_u}_{\boldsymbol{F}_e^m}, \tag{37}$$

thus

$$\boldsymbol{f}_e^m = \boldsymbol{\mathcal{S}}_{eu}^m\boldsymbol{f}_u, \tag{38}$$

$$\boldsymbol{F}_e^m = \boldsymbol{\mathcal{S}}_{eu}^m\boldsymbol{F}_u. \tag{39}$$

Consider now the influence of the type of moving load. Its work W can be written for each element as

$$W = \boldsymbol{T}_W \boldsymbol{\Phi} = \underbrace{\boldsymbol{T}_W \boldsymbol{\Psi}}_{\boldsymbol{D}} \boldsymbol{d}_e, \tag{40}$$

where $\boldsymbol{T}_W = \boldsymbol{T}_W(y,z)$ is a row vector, detailed in Section 3.4, and the row vector $\boldsymbol{D}$ is precisely $\boldsymbol{F}_e^m$ due to work conjugacy. Substituting in Eq. (37) and using Eq. (38), the influence surface on element m is provided by

$$f^m = \boldsymbol{D}\boldsymbol{f}_e^m = \boldsymbol{T}_W \boldsymbol{\Psi} \boldsymbol{S}_{eu}^m \boldsymbol{f}_u. \tag{41}$$

For clarity, the procedure for obtaining influence surfaces is summarized next. First, a GBT-based finite element model of the structure is established; $\boldsymbol{K}_e$ and $\boldsymbol{K}_u$ are calculated. Then, for each effect and moving load:

1. calculate $\boldsymbol{T}_f$;
2. solve Eq. (36) for $\boldsymbol{f}_u$;
3. obtain the expression for $\boldsymbol{T}_W$;
4. The influence surface for each element is computed with Eq. (41).

Only step 2 requires a computational effort, but it is equivalent to that of a standard linear analysis. Note that this step does not depend on the type of moving loads nor requires changing the model.

Finally, it is remarked that a decrease of accuracy of the influence surface is expected in the element where the sought effect is calculated, since the element is acted by equivalent nodal forces (vector $\boldsymbol{T}_f^T$).

3.3. The expressions for $\boldsymbol{T}_f$

The row vector $\boldsymbol{T}_f$ allows calculating the sought effect from the element DOFs. This vector is constant-valued, since x, y, z correspond to the coordinates of the point where the effect is calculated in the target element. The general form can be written as

$$\boldsymbol{T}_f = \boldsymbol{e}_k^T \boldsymbol{\Xi}_{\boldsymbol{T}_f} \boldsymbol{\Psi}_f, \tag{42}$$

where k corresponds to the desired component of matrix $\boldsymbol{\Xi}_{\boldsymbol{T}_f}$, which depends on the effect as explained next. Both $\boldsymbol{\Xi}_{\boldsymbol{T}_f}$ and $\boldsymbol{\Psi}_f$ are evaluated only for the coordinates of the point where the effect is measured (the subscript f is used to emphasize this point).

Matrix $\boldsymbol{\Xi}_{\boldsymbol{T}_f}$ can be found by comparing the expression of the sought effect with the substitution of Eq. (42) in Eq. (34),

$$f = \boldsymbol{e}_k^T \boldsymbol{\Xi}_{\boldsymbol{T}_f} \boldsymbol{\Psi}_f \boldsymbol{d}_e^n = \boldsymbol{e}_k^T \boldsymbol{\Xi}_{\boldsymbol{T}_f} \boldsymbol{\Phi}_f, \tag{43}$$

which leads to:

(i) For displacements, from Eq. (5),

$$\boldsymbol{\Xi}_{\boldsymbol{T}_f} = \boldsymbol{\Xi}_{\boldsymbol{U}}, \tag{44}$$

and $k = 1, 2, 3$. For instance, for U_y, i.e. the second component of the displacement vector, one adopts $k = 2$ and thus $\boldsymbol{e}_2^T = [0\ 1\ 0]$.

(ii) For rotations, which can be calculated with [17]

$$\begin{bmatrix} \theta_x \\ \theta_y \end{bmatrix} = \boldsymbol{\Xi}_\theta \boldsymbol{\Phi}, \quad \boldsymbol{\Xi}_\theta = \begin{bmatrix} \bar{\boldsymbol{w}}_{,y}^T & \boldsymbol{0} & \boldsymbol{0} \\ \boldsymbol{0} & -\bar{\boldsymbol{w}}^T & \boldsymbol{0} \end{bmatrix}, \tag{45}$$

one immediately identifies

$$\boldsymbol{\Xi}_{\boldsymbol{T}_f} = \boldsymbol{\Xi}_\theta, \tag{46}$$

and one uses $k = 1$ for θ_x and $k = 2$ for θ_y.

(iii) For strains or stresses, from (7) or (9),

$$\boldsymbol{\Xi}_{\boldsymbol{T}_f} = \boldsymbol{\Xi}_{\boldsymbol{\epsilon}}, \tag{47}$$

$$\boldsymbol{\Xi}_{\boldsymbol{T}_f} = \boldsymbol{\Xi}_{\boldsymbol{\sigma}}, \tag{48}$$

respectively, and $k = 1, 2, 3$. For instance, for γ_{xy} or σ_{xy}, $k = 3$ and $\boldsymbol{e}_3^T = [0\ 0\ 1]$.

(iv) For stress resultants, from Eq. (16),

$$\boldsymbol{\Xi}_{\boldsymbol{T}_f} = \boldsymbol{\mathcal{M}} \tag{49}$$

and in this case $k = 1, \ldots, 3D$. For instance, for the bimoment associated with deformation mode 5, $\mathcal{X}_{xx}^{(5)}$, one uses $k = 2D + 5$.

(v) The amplitude of a particular deformation mode or its derivatives (recall that the warping displacements depend on ϕ_k') may also constitute a sought effect. In this case $\boldsymbol{\Xi}_{\boldsymbol{T}_f}$ is the $3D \times 3D$ identity matrix and $k = 1, \ldots, 3D$, with $k = 1, \ldots, D$ used for calculating ϕ_1 to ϕ_D, $k = D+1, \ldots, 2D$ for ϕ_1' to ϕ_D' and $k = 2D+1, \ldots, 3D$ for ϕ_1'' to ϕ_D''.

Reactions at nodes can be calculated from the connecting element nodal DOFs, thus in this case the format is different,

$$\boldsymbol{T}_f = \boldsymbol{e}_k^T \boldsymbol{K}_e, \tag{50}$$

where k specifies the sought DOF. Since the forces applied at restrained DOFs do not produce displacements, a particular solution must be added, as explained in the next Section.

3.4. The expressions for $\boldsymbol{T}_W$

The row vector $\boldsymbol{T}_W$ accounts for the moving load type and can be established by work equivalence, from Eq. (40). It is remarked that $\boldsymbol{T}_W$ is not constant-valued, as y, z vary according to the load path considered, and that the variation along x is provided by $\boldsymbol{\Psi}$ in Eq. (40).

The most common case corresponds to a moving concentrated force $\boldsymbol{P}$. If the force is defined along the local axes,

$$\boldsymbol{T}_W = \boldsymbol{P}^T \boldsymbol{\Xi}_U. \tag{51}$$

For moving moments acting at the midsurface, along the local axes,

$$\boldsymbol{T}_W = \begin{bmatrix} M_x & M_y \end{bmatrix} \boldsymbol{\Xi}_\theta. \tag{52}$$

It is also possible to define section-wise loads moving along the beam axis, in which case influence lines are obtained. Loads which are work-conjugate to the amplitude of a given deformation mode (or its derivatives) can be considered, through

$$\boldsymbol{T}_W = \boldsymbol{e}_k^T, \tag{53}$$

with $k = 1, \ldots, D$ for ϕ_1 to ϕ_D, $k = D+1, \ldots, 2D$ for ϕ_1' to ϕ_D' and $k = 2D+1, \ldots, 3D$ for ϕ_1'' to ϕ_D''. Note that in this case $\boldsymbol{D}$ becomes a function of x only, thus leading to an influence line.

As mentioned in Section 3.3, for reaction influence functions a particular solution must be added to that provided by Eq. (41), for the target elements. This solution corresponds to the symmetric of the component of the element load vector ($\boldsymbol{F}_e = \boldsymbol{D}$) corresponding to the sought reaction. The solution (41) in those elements must therefore be amended to

$$f^m = \boldsymbol{D}\boldsymbol{S}_{eu}^m \boldsymbol{f}_u - \boldsymbol{e}_k^T \boldsymbol{D} = \boldsymbol{D}\left(\boldsymbol{S}_{eu}^m \boldsymbol{f}_u - \boldsymbol{e}_k\right), \tag{54}$$

where k specifies the DOF corresponding to the reaction.

3.5. Comparison with reciprocity-based solutions

It is worth comparing the proposed method with the standard method that relies on Betti's reciprocal work theorem. With the proposed method, collecting all relevant equations, the influence surface on element m is given by

$$f^m = \boldsymbol{T}_W \boldsymbol{\Psi} \boldsymbol{S}_{eu}^m \boldsymbol{K}_u^{-1} \boldsymbol{P}_{eu}^n \boldsymbol{\Psi}_f^T \boldsymbol{\Xi}_{\boldsymbol{T}_f}^T \boldsymbol{e}_k. \tag{55}$$

Using Betti's theorem, the influence surface for a generalized displacement ($\boldsymbol{U}$, θ_x, θ_y, ϕ_k or ϕ_k') corresponds to the displacement that is work conjugate to the moving load, generated by a load which is work conjugate to the sought generalized displacement. This corresponds precisely to Eq. (55) since:

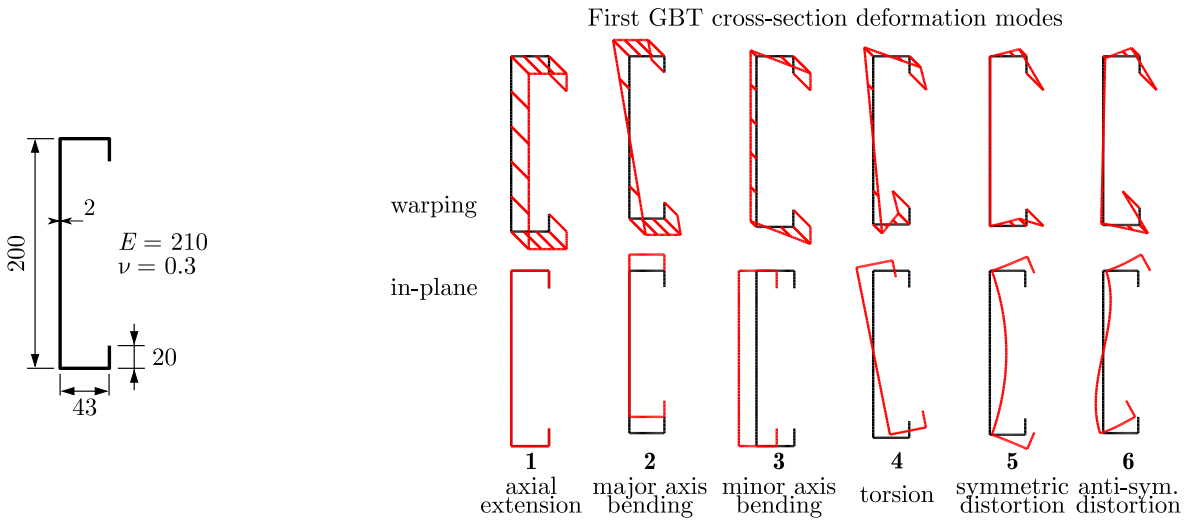

Fig. 2. Lipped channel geometry (mid-line dimensions), material parameters and first GBT cross-section deformation modes.

- $\mathcal{P}^n_{eu}\Psi^T_f\Xi^T_{T_f}e_k$ is the load which is work conjugate to the sought generalized displacement. Matrix Ξ_{T_f} equals (i) Ξ_U for displacements, (ii) Ξ_θ for rotations and (iii) the identity matrix for ϕ_k and ϕ'_k.
- pre-multiplying the load by K_u^{-1} returns the corresponding displacement vector.
- pre-multiplying the displacement vector by $T_W\Psi S^m_{eu}$ provides the displacement that is work conjugate to the moving load at element m, as a function of x (through Ψ) and y (through T_W).

3.6. Modal decomposition

Owing to the unique features of GBT, it is possible to perform a mode decomposition of the influence surfaces. Let matrix B^k filter the entries of vector $f = \mathcal{P}_u f_u$ pertaining to deformation mode k,

$$f^k = B^k f, \tag{56}$$

such that

$$f = \sum_{k=1}^{D} f^k \quad \Rightarrow \quad \sum_{k=1}^{D} B^k = \mathbf{1}, \tag{57}$$

where $\mathbf{1}$ is an identity matrix. This allows defining influence surfaces for each deformation mode k and element m, through

$$f^{m,k} = D S^m_e f^k, \tag{58}$$

which for reactions should be corrected according to Eq. (54). It is remarked that

Remark 3.3. $f^{m,k}$ is the contribution of deformation mode k to the influence surface (in element m), as f^m can be obtained by adding all $f^{m,k}$.

Scalar measures of the participation of each mode in the solution can be also introduced, as shown in Section 4.1.

4. Illustrative examples

A series of examples are presented next, to illustrate the capabilities of the proposed method. In all cases consistent units are employed. In the GBT approach, this implies $\bar{u}_k$, $\bar{v}_k$, $\bar{w}_k$ in $[L]$, ϕ_k [-], $\mathcal{X}^k_{xx}$ in $[FL^2]$, $\mathcal{X}^k_{yy}$ in $[F]$ and $\mathcal{X}^k_{xy}$ in $[FL]$. Uniform finite element meshes are always adopted, even if it is already expected that the error is only significant in the target element.

4.1. Lipped channel beams

The first example concerns beams with the lipped channel cross-section geometry and material parameters displayed in Fig. 2, which also shows the most relevant GBT cross-section deformation modes: axial extension (1), major- and minor-axis bending (2,3), torsion (4) and distortion (5,6). The modes are calculated using GBTUL [19], which is freely available from https://sites.fct.unl.pt/gbt/.

Fig. 3 presents a few standard influence lines for two well-known cases: (a) a simply supported beam and (b) a two-span beam. The beams are subjected to a moving vertical downward force, applied along the top flange-lip fold. The analyses are first carried out with the rigid-body modes 1–4 and, when mentioned, also mode 17, the shear counterpart to the major-axis bending mode 2 (mode 17 corresponds to the warping component of mode 2).

Fig. 3(a) shows the influence lines for (i) major axis bending ($\mathcal{X}_{xx}$ for mode 2) at mid-span, (ii) the shear force ($\mathcal{X}_{xy}$ for mode 17) at mid-span and (iii) the vertical reaction at the left support. The mid-span effect is calculated at the element immediately to its left. The error is calculated by evaluating the functions at $i = 1, \ldots, 129$ equally spaced points and using

$$e = \frac{\sum_{i=1}^{129} |f_i - f_{i,exact}|}{\sum_{i=1}^{129} |f_{i,exact}|}, \tag{59}$$

where $f_{i,exact}$ is the exact solution. These results prompt the following remarks:

(i) Concerning the bending moment, the solution is exact except at the target element, as already anticipated. However, the error quickly vanishes as the number of elements increases.

(ii) For the shear force the error is not confined to the target element and a low error requires many elements (the convergence is of order 1 in this case). This stems from the standard GBT kinematics, which are based on an Euler–Bernoulli description of bending (C^1 interpolation of the beam axis) and does not allow discontinuity of slopes of the axis even if the shear mode 17 is included.[1] However, if only the end-points of each element are used, as shown in the bottom-right of the graph, much more

[1] Possible solutions include adopting a Timoshenko-type description or enforcing continuity at nodes connecting two elements in terms of total displacements (not for each deformation mode separately), to allow slope discontinuities at nodes.

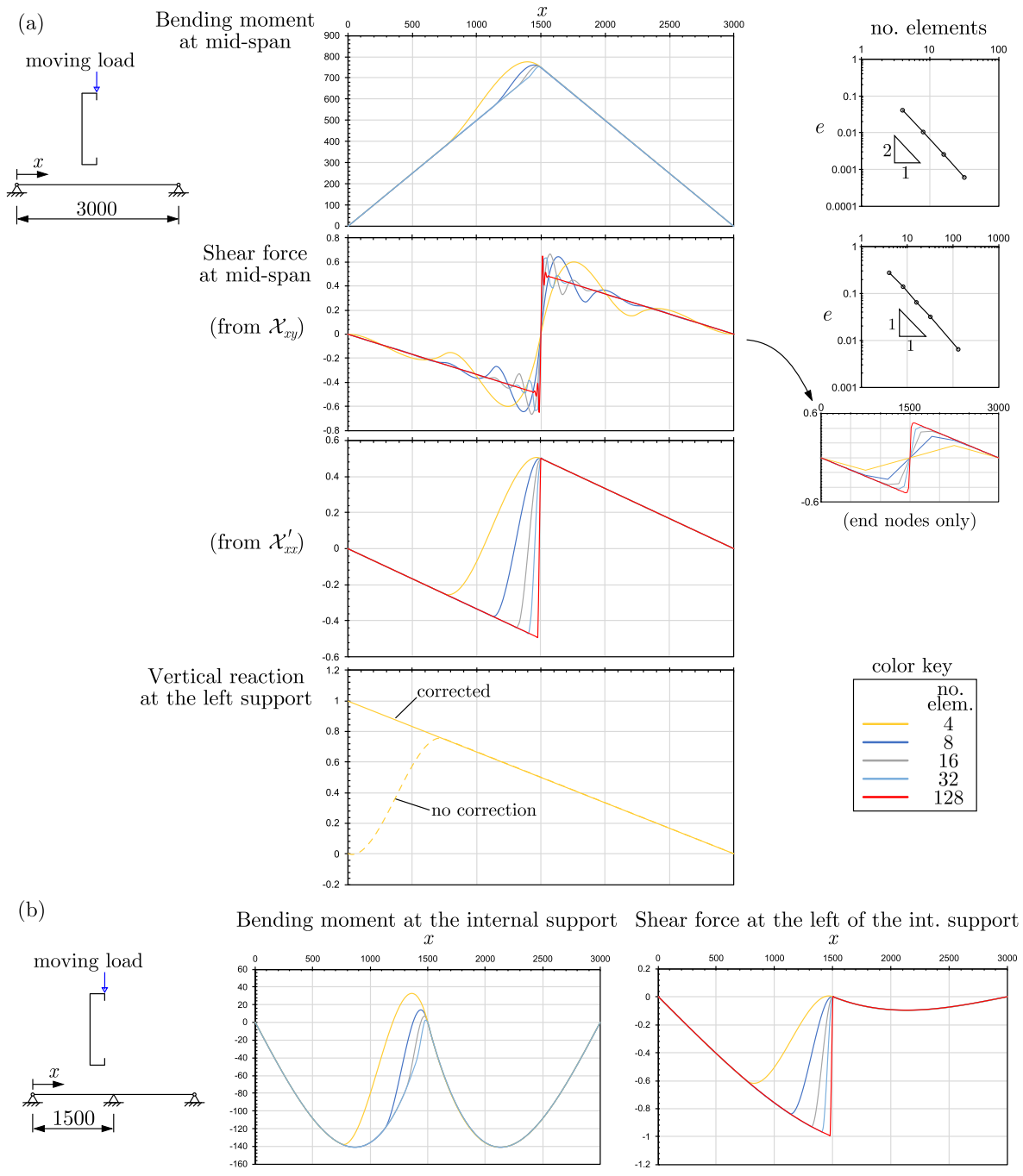

Fig. 3. Standard influence lines for lipped channel (a) simply supported and (b) two-span beams.

accurate solutions are obtained. In alternative, the influence line can be obtained by calculating the shear force from the derivative of the bending moment,

$$\mathcal{X}_{xy}^{(17)} = \left(\mathcal{X}_{xx}^{(2)}\right)' \quad \Rightarrow \quad \boldsymbol{T}_f = \boldsymbol{e}_k^T \boldsymbol{\mathcal{M}} \boldsymbol{\Psi}', \tag{60}$$

with $k = 2D + 2$. The results are also shown in the figure and a much more accurate solution is obtained, exhibiting differences with respect to the exact solution only at the target element.

(iii) The vertical reaction influence line is exact, even for a single element (the figure shows the solution for 4 elements), provided that the correction of Eq. (54) is included. Without it, the value at the support is null, since the vertical displacement is restrained.

Fig. 3(b) displays the influence lines for the bending moment over the internal support (left graph) and the shear force at the left of the support (right graph), the latter obtained from the derivative of the bending moment. Excellent results are once more obtained and, although not shown, the convergence features are qualitatively similar to those in Fig. 3.

Attention is now turned to non-standard influence lines and surfaces. Fig. 4 shows results for a cantilever beam discretized using 15 elements and modes 1 to 6 (thus two distortions are considered).

The top left graphs show the non-null influence lines for $\mathcal{X}_{xx}$ at the support (those for modes 1 and 3 are obviously null). The exact solution for mode 2 is recovered, with a slight deviation at the target element (next to the support), as already pointed out. The highest values are

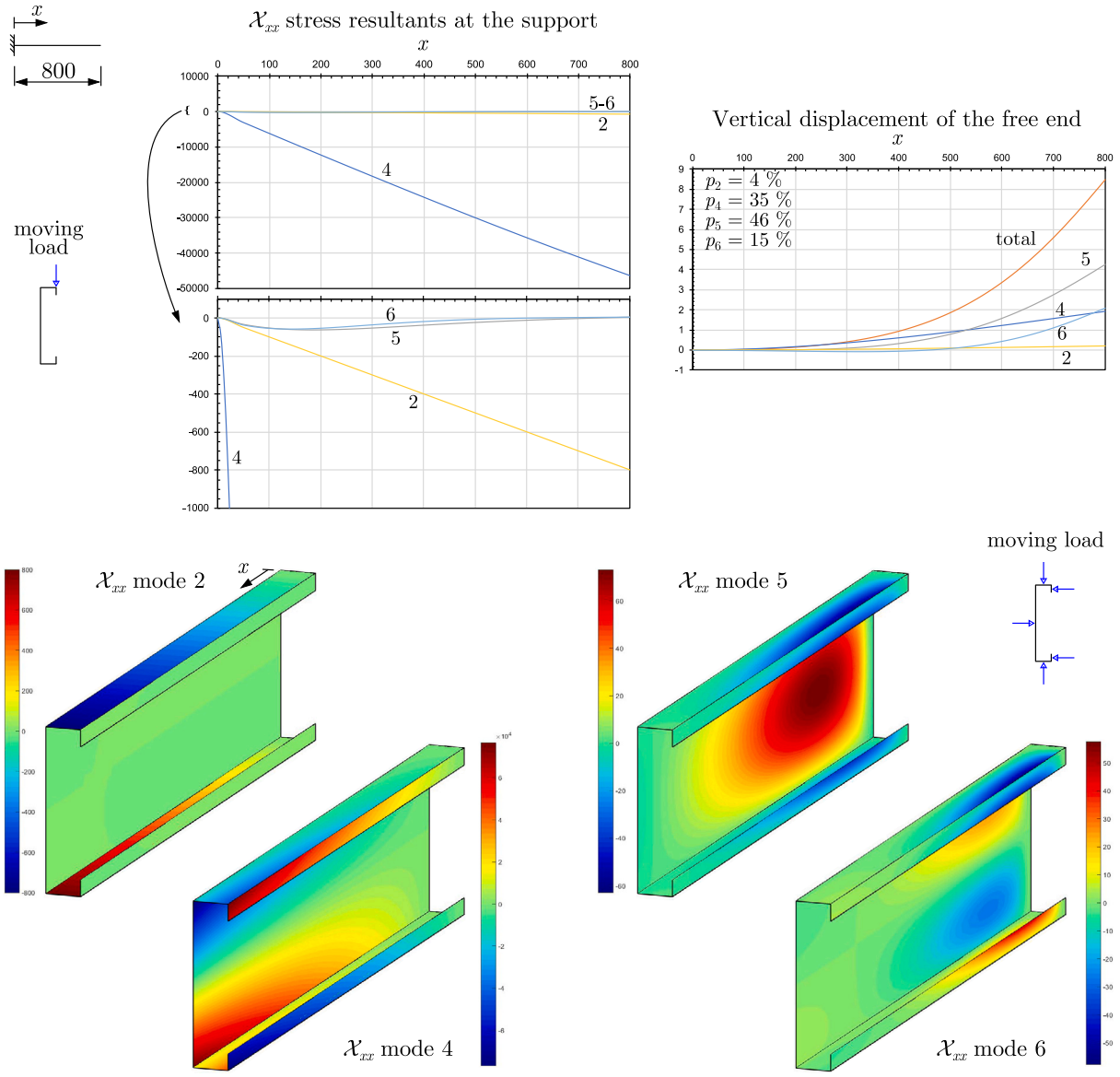

Fig. 4. Cantilever lipped channel beam.

obtained for the bimoment (mode 4), which generates an almost linear function having its maximum at the free end and falling within 2.5% of the analytical solution

$$B = \frac{T \tanh(\alpha L)}{\alpha}, \quad \alpha = \sqrt{\frac{(\mathsf{D}_1)_{(4,4)}}{\mathsf{C}_{(4,4)}}}, \tag{61}$$

with $T = 62.1$ due to the eccentricity of the load with respect to the shear center, where $\mathsf{C}_{(4,4)}$ is the warping stiffness and $(\mathsf{D}_1)_{(4,4)}$ is the St. Venant torsion stiffness. Even though the difference with respect to the analytical solution is very small, it is worth remarking that it stems from torsion–distortion coupling effects. In fact, when distortion is removed from the analysis, the difference drops to less than 0.005%. Both distortional bimoments have quite non-linear influence lines, which are negative almost throughout the length, slightly on the positive side near the free end.

The right graph in Fig. 4 shows the influence line for the vertical displacement of the free end point of load application, and its modal breakdown according to Eq. (58), as well as the corresponding participations calculated using

$$p^k = \frac{\int_{\mathcal{L}} f^k \, \mathrm{d}\mathcal{L}}{\int_{\mathcal{L}} f \, \mathrm{d}\mathcal{L}}, \tag{62}$$

where the integrations are carried out in the load path $\mathcal{L}$.[2] Mode 5 (symmetric distortion) plays the most significant role (46%), even if torsion and anti-symmetric distortion are also quite relevant. Note however that the hierarchy changes with the position of the load. For instance, while the distortional modes are the most relevant for a load

[2] Using previous relations,

$$\int_{\mathcal{L}} f^k \, \mathrm{d}\mathcal{L} = \boldsymbol{E}\boldsymbol{B}^k \boldsymbol{f},$$

$$\boldsymbol{E} = \sum_m \int_{\mathcal{L}} \boldsymbol{T}_W^m \mathrm{d}y\mathrm{d}z \int_{\mathcal{L}} \boldsymbol{\Psi}^m \mathrm{d}x \; \boldsymbol{S}_e^m,$$

therefore one obtains

$$p^k = \frac{\boldsymbol{E}\boldsymbol{B}^k \boldsymbol{f}}{\boldsymbol{E}\boldsymbol{f}}.$$

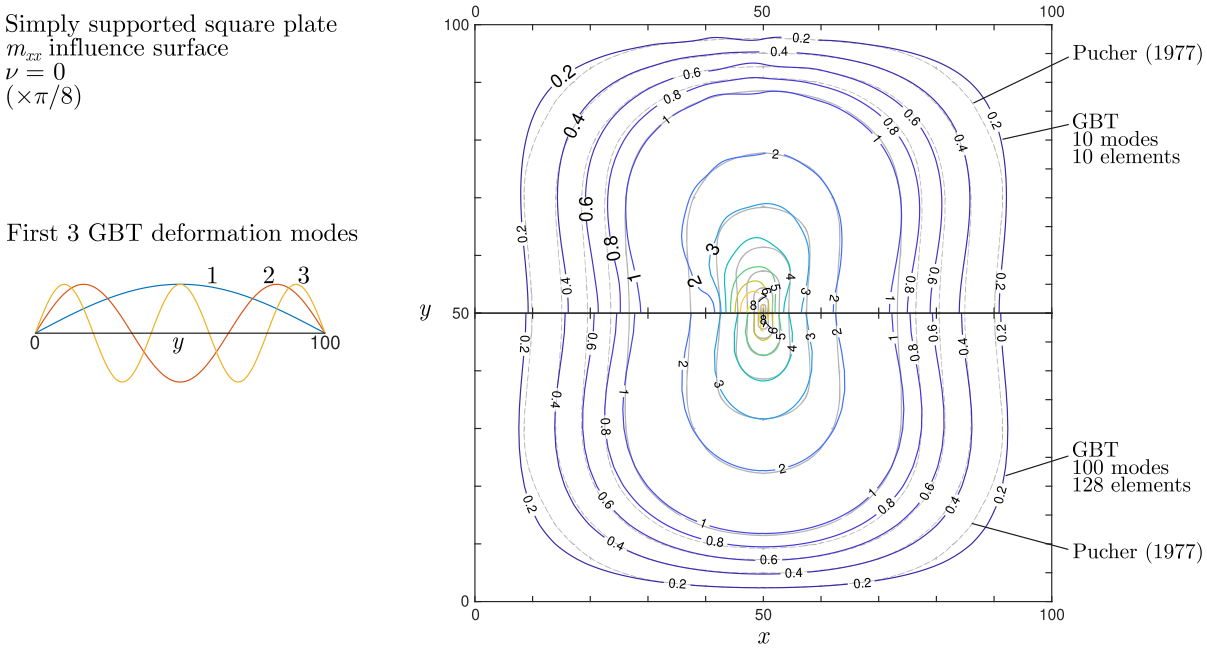

Fig. 5. Influence surface of m_{xx} for a simply supported square plate.

at $x = 800$, they quickly damp out as x decreases and mode 4 (torsion) becomes dominant for $x < 530$.

The bottom part of the figure displays the influence surfaces for the stress resultants, considering that the moving load acts perpendicularly to the walls, as shown in the figure. Note that the previous influence lines correspond to these surfaces at the top flange-lip fold. These surfaces make it possible to identify the most unfavorable positions of the loads for each resultant: at the free end for bending and torsion; close to the support for distortion.

4.2. Influence surfaces for plates

GBT can be also used to obtain influence surfaces for flat plates. Fig. 5 concerns a square plate with all edges simply supported, and shows the isolines of the mid-span moment influence surface obtained by Pucher [2] (gray lines) and with the proposed GBT-based approach (colored lines) using two discretization levels: (i) 10 modes and 10 elements (upper part), and (ii) 100 modes and 128 elements (lower part). The GBT deformation modes used correspond to sinusoidal functions with an increasing even number of half-waves, as in [20,21] — the first three modes are shown in the figure. The results show that the GBT surfaces are in very good agreement with that in [2], but obtaining an accurate solution at mid-span requires the most refined discretization.

4.3. Stiffened plate

Consider the simply supported stiffened plate shown in Fig. 6. The cross-section is discretized by subdividing the plate (not the stiffeners) into sixteen 250-length segments, leading to the deformation modes displayed in the figure (only the first three local-plate modes are shown and the warping component of the rigid-body and distortional modes is omitted for simplicity), which were obtained using GBTUL.

A downward vertical moving load is applied at the plate mid-surface and the shear lag effect at mid-span is investigated, by calculating the influence surface of the difference between the mid-span longitudinal membrane strains at points A and B in the figure,

$$f = \left(\varepsilon_{xx}^{M}\right)_A - \left(\varepsilon_{xx}^{M}\right)_B . \tag{63}$$

The results are shown in the bottom part of Fig. 6. The surface is calculate using modes 1–31 (rigid-body, distortional and local-plate) and all modes 1–59 (adding the shear modes), and 128 finite elements, to ensure accurate results.

When only modes 1–31 are included, the surface is anti-symmetric with respect to $y = 2000$ and is exclusively due to the torsion-related bimoment, i.e. the remaining modes do not have significant participations. When all modes are included, the surface is significantly changed due to the shear lag effect, exhibiting a peak at mid-span, for $y \approx 1500$.

4.4. Curved box-girder bridge

The final example concerns a simply supported concrete box girder bridge with the cross-section and material parameters shown in Fig. 7(a), taken from [22]. The prismatic case was analyzed using GBT in [18] and excellent results were obtained. For illustrative purposes, Fig. 7(b) shows the mid-surface stresses σ_{xx}^{M} at mid-span, obtained with 30 GBT-based finite elements and 1800 4-node shell finite elements, using ADINA [23], evidencing an excellent match.

Influence surfaces for the amplitude of distortion (mode 5) at mid-span are calculated. Diaphragms constraining distortion are provided at the supports, $L/3$ and $2L/3$, to obtain a non-trivial surface shape, and the moving loads are assumed to act perpendicular to all walls. Besides the prismatic case, 45° and 90° horizontally curved bridges with the same span are also analyzed, to assess the effect of the axis curvature. A uniform discretization using 12 elements proved to be adequate.

It is recalled that the GBT for curved members and a suitable finite element were presented and described in detail in [24,25]. Even though the deformation modes depend on the axis curvature, as shown in Fig. 7(c), their normalization criteria is the same, to allow meaningful comparisons. In particular, the distortional mode 5 is normalized by setting the maximum in-plane displacement to 1.

The influence surfaces are shown in Fig. 8. For the prismatic case, as expected, the surfaces are symmetric with respect to mid-span and anti-symmetric with respect to the vertical plane passing through the longitudinal axis. For the curved case, while the mid-span symmetry is maintained, the anti-symmetry is lost. In fact, as the curvature increases, the effect increases at regions between the longitudinal axis

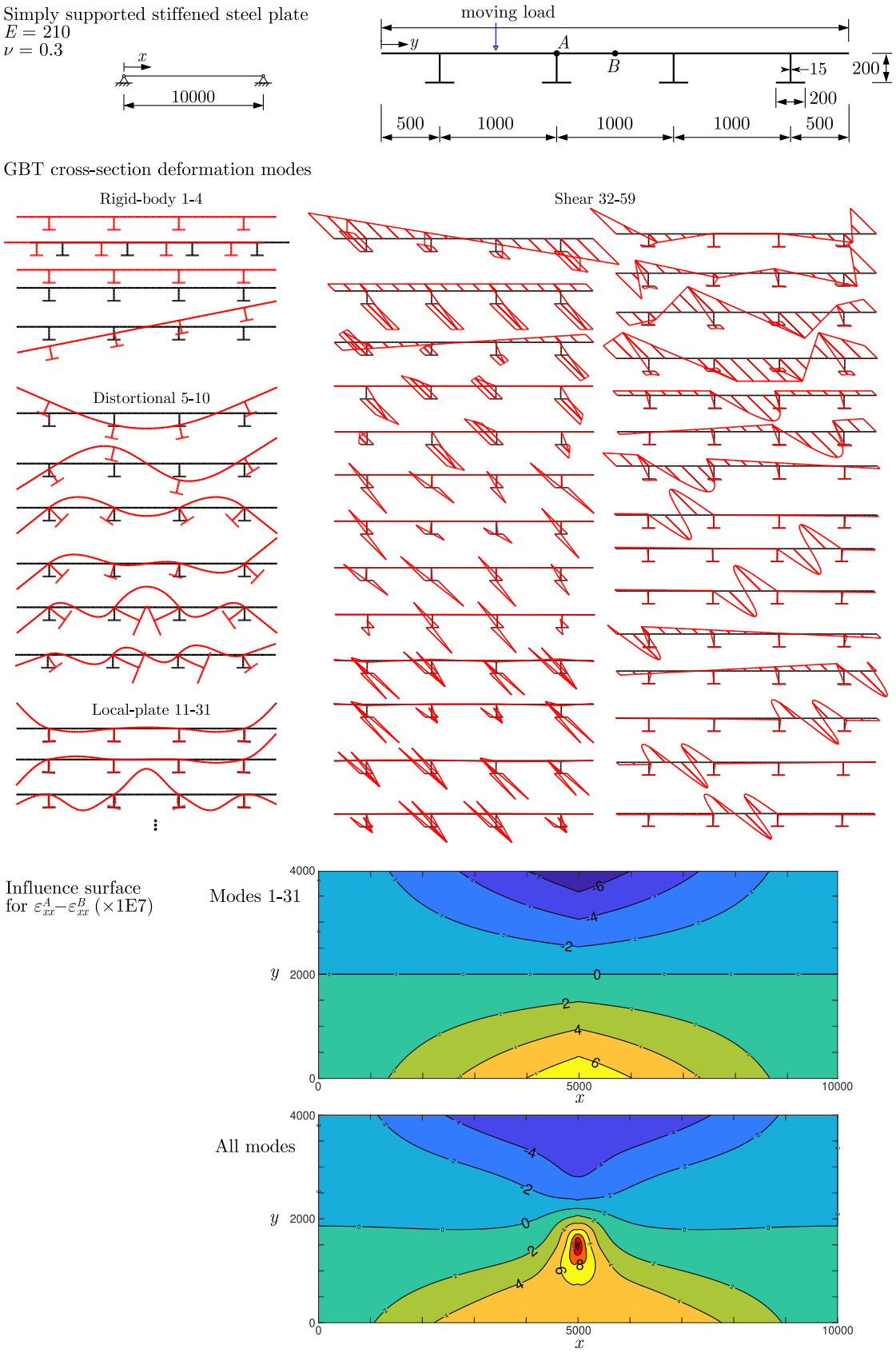

Fig. 6. Stiffened plate geometry, material parameters, GBT deformation modes and influence surfaces for $f = \left(\epsilon^M_{xx}\right)_A - \left(\epsilon^M_{xx}\right)_B$ at mid-span.

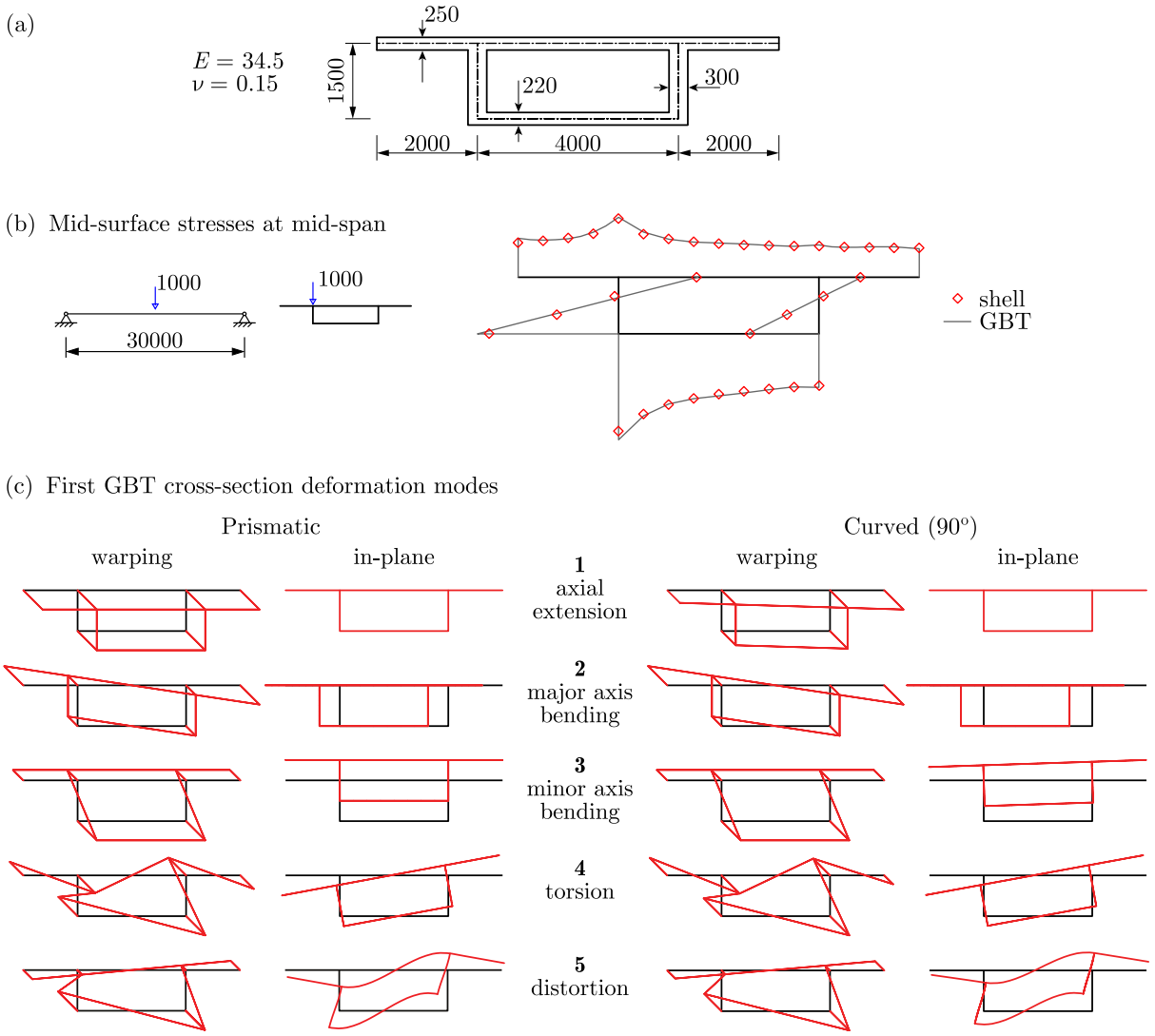

Fig. 7. Concrete box girder bridge (a) cross-section geometry and material parameters, (b) mid-span stresses [18] and (c) first GBT deformation modes for the prismatic and 90° cases.

and the curvature center (e.g. the blue zones maximum increases in absolute value), while decreasing at the deck slab regions located farther from the curvature center (e.g. the maximum red value at this wall decreases). It is therefore concluded that distortion effects increase as the curvature increases, provided that the load is applied in a point between the longitudinal axis and the curvature center.

It is also worth noting the "checkerboard" pattern of the influence surfaces (more evident in the prismatic case), which is due to the presence of the diaphragms, which restrain distortion and thus null values of the surface at their locations ($x = 0, L/3, 2L/3$ and L).

Further insight can be gained from the modal decomposition of the solution. For illustrative purposes, Fig. 9 shows the non-null contributions for the 90° case, being worth remarking that the color range is the same for all surfaces, to facilitate the comparison. A major contribution from distortion is observed, which is expected since distortion is the sought effect, together with a small contribution from torsion (torsion and distortion couple in box-girders) and a significant contribution from minor-axis bending (torsion and out-of-plane bending couple in curved members).

5. Concluding remarks

This paper introduced a GBT-based method for the calculation of influence functions (lines and surfaces) for thin-walled members. Attention is called to the following aspects of the proposed method:

(i) The computational cost of the calculation procedure is equivalent to that of a single linear analysis of the structure and does not depend on the type of moving load nor requires changing the model.
(ii) Besides the standard influence functions, non-standard ones can be calculated, pertaining to higher-order cross-section deformation modes (e.g. distortion) and the associated stress resultants.
(iii) A modal decomposition of the influence function can be performed through straightforward post-processing, providing valuable structural insight.

The capabilities of the proposed method were illustrated in several examples, comprising lipped channel beams, a square plate, a longitudinally stiffened plate and straight/curved box-girder bridge.

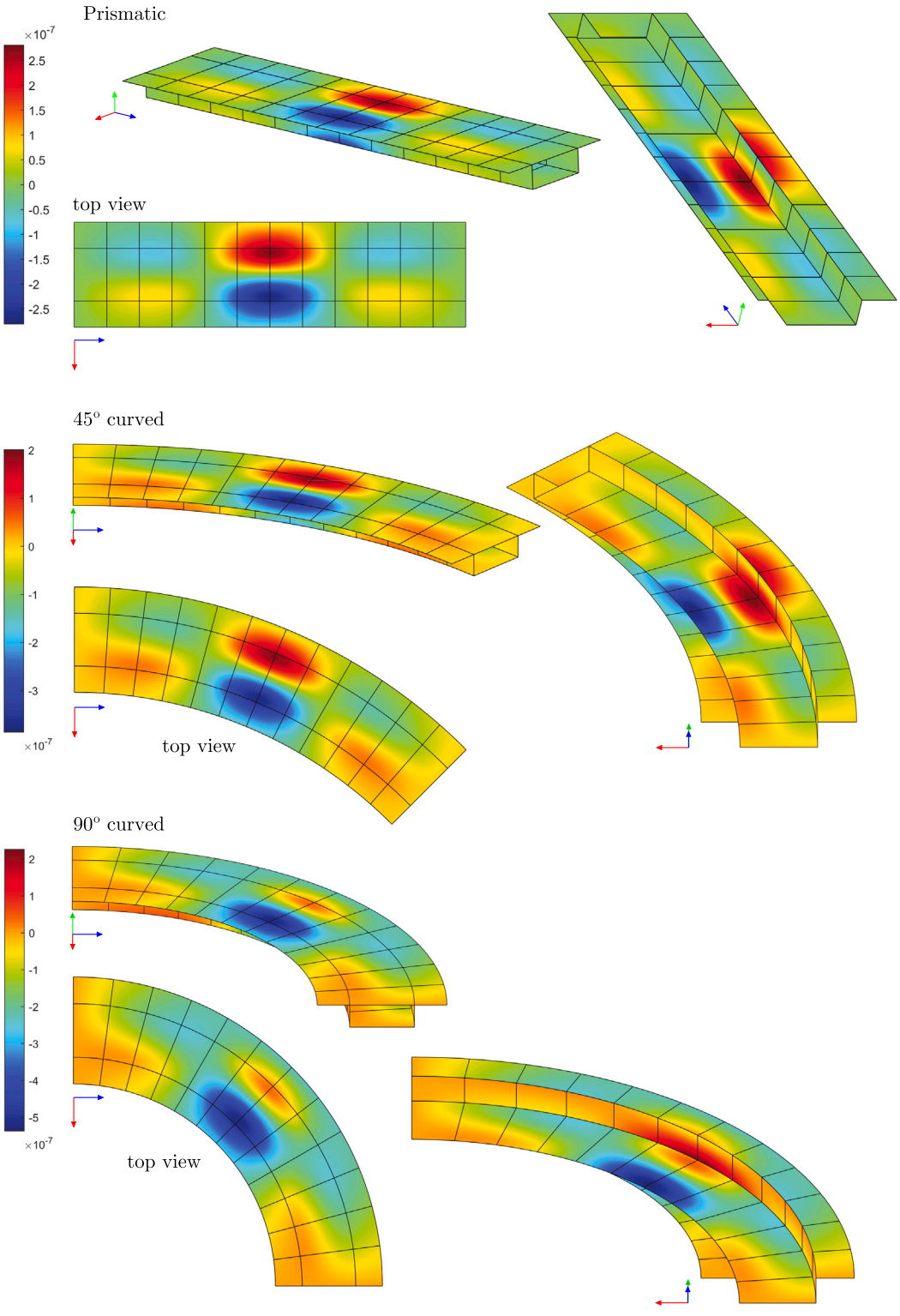

Fig. 8. Concrete box-girder bridge influence surfaces for the amplitude of distortion (mode 5) at mid-span.

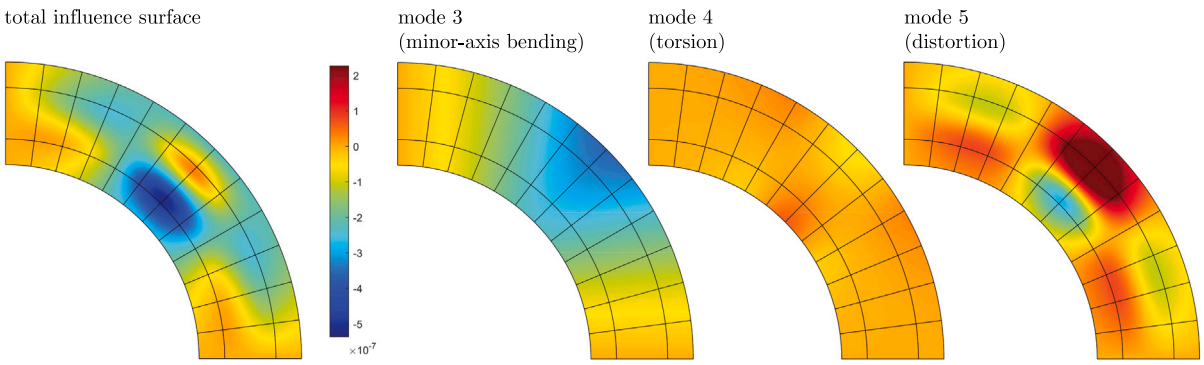

Fig. 9. Decomposition of the influence surface for the amplitude of distortion at mid-span.

Although the proposed method is GBT-based, the authors hope this paper paves the way for its application to other higher-order thin-walled beam models that account for arbitrary cross-section deformation through appropriate deformation modes, such as those in [26–29].

CRediT authorship contribution statement

David Henriques: Investigation. **Nuno Peres:** Investigation. **Rodrigo Gonçalves:** Investigation.

Declaration of competing interest

The authors declare that they have no known competing financial interests or personal relationships that could have appeared to influence the work reported in this paper.

Acknowledgment

The second and third authors are grateful for the Foundation for Science and Technology's support through funding UIDB/04625/2020 from the research unit CERIS (DOI:10.54499/UIDB/04625/2020).

References

[1] Timoshenko S, Woinowsky-Krieger S. Theory of plates and shells. McGraw-Hill; 1959.
[2] Pucher A. Einflußfelder elastischer Platten / influence Surfaces of Elastic Plates. Springer Vienna; 1977, http://dx.doi.org/10.1007/978-3-7091-7070-0.
[3] Cifuentes A, Paz M. A note on the determination of influence lines and surfaces using finite elements. Finite Elem Anal Des 1991;7(4):299–305. http://dx.doi.org/10.1016/0168-874x(91)90045-z.
[4] Fu H-c. Indirect structural analysis by finite element method. J Struct Div 1973;99(1):91–111. http://dx.doi.org/10.1061/jsdeag.0003439.
[5] Belegundu A. The adjoint method for determining influence lines. Comput Struct 1988;29(2):345–50. http://dx.doi.org/10.1016/0045-7949(88)90269-6.
[6] Memari A, West H. Computation of bridge design forces from influence surfaces. Comput Struct 1991;38(5–6):547–56. http://dx.doi.org/10.1016/0045-7949(91)90006-8.
[7] Orakdogen E, Girgin K. Direct determination of influence lines and surfaces by F.E.M.. Struct Eng Mech 2005;20(3):279–92.
[8] Jepsen MS, Damkilde L. A direct and fully general implementation of influence lines/surfaces in finite element software. Adv Eng Softw 2018;120:55–61. http://dx.doi.org/10.1016/j.advengsoft.2016.04.006.
[9] Schardt R. Eine erweiterung der technischen biegetheorie zur berechnung prismatischer faltwerke. Stahlbau 1966;35:161–71, (German).
[10] Schardt R. Verallgemeinerte Technische Biegetheorie. Berlin, Germany: Springer Verlag; 1989, (German).
[11] Gonçalves R, Camotim D, Basaglia C, Martins AD, Peres N. Latest developments on the analysis of thin-walled structures using generalised beam theory (GBT). J Constr Steel Res 2023;204:107858. http://dx.doi.org/10.1016/j.jcsr.2023.107858.
[12] Gonçalves R, Camotim D. Generalised beam theory-based finite elements for elastoplastic thin-walled metal members. Thin-Walled Struct 2011;49(10):1237–45. http://dx.doi.org/10.1016/j.tws.2011.05.011.
[13] Gonçalves R, Ritto-Corrêa M, Camotim D. A new approach to the calculation of cross-section deformation modes in the framework of generalized beam theory. Comput Mech 2010;46(5):759–81. http://dx.doi.org/10.1007/s00466-010-0512-2.
[14] Gonçalves R, Bebiano R, Camotim D. On the shear deformation modes in the framework of Generalized Beam Theory. Thin-Walled Struct 2014;84:325–34. http://dx.doi.org/10.1016/j.tws.2014.07.012.
[15] Bebiano R, Gonçalves R, Camotim D. A cross-section analysis procedure to rationalise and automate the performance of GBT-based structural analyses. Thin-Walled Struct 2015;92:29–47. http://dx.doi.org/10.1016/j.tws.2015.02.017.
[16] Gonçalves R, Camotim D. Geometrically non-linear generalised beam theory for elastoplastic thin-walled metal members. Thin-Walled Struct 2012;51:121–9. http://dx.doi.org/10.1016/j.tws.2011.10.006.
[17] Manta D, Gonçalves R, Camotim D. On the compatibility between reissner–mindlin shell and GBT-based finite elements. Thin-Walled Struct 2023;192:111150. http://dx.doi.org/10.1016/j.tws.2023.111150.
[18] Vieira L. Longitudinal analysis of steel-concrete composite box girder decks: comparison between the classical formulations and the generalized beam theory. Master's thesis, Técnico Lisboa; 2017.
[19] Bebiano R, Camotim D, Gonçalves R. GBTUL 2.0 - a second-generation code for the GBT-based buckling and vibration analysis of thin-walled members. Thin-Walled Struct 2018;124:235–57. http://dx.doi.org/10.1016/j.tws.2017.12.002.
[20] Gonçalves R, Camotim D. GBT local and global buckling analysis of aluminium and stainless steel columns. Comput Struct 2004;82(17–19):1473–84. http://dx.doi.org/10.1016/j.compstruc.2004.03.043.
[21] Gonçalves R, Le Grognec P, Camotim D. GBT-based semi-analytical solutions for the plastic bifurcation of thin-walled members. Int J Solids Struct 2010;47(1):34–50. http://dx.doi.org/10.1016/j.ijsolstr.2009.09.013.
[22] Maisel BI, Roll F. Methods of analysis and design of concrete box beams with side cantilevers. Cement and Concrete Association; 1974.
[23] Bathe KJ. ADINA system. 2016.
[24] Peres N, Gonçalves R, Camotim D. First-order generalised beam theory for curved thin-walled members with circular axis. Thin-Walled Struct 2016;107:345–61. http://dx.doi.org/10.1016/j.tws.2016.06.016.
[25] Peres N, Gonçalves R, Camotim D. GBT-based cross-section deformation modes for curved thin-walled members with circular axis. Thin-Walled Struct 2018;127:769–80. http://dx.doi.org/10.1016/j.tws.2018.03.008.
[26] Hodges DH. Nonlinear composite beam theory. American Institute of Aeronautics and Astronautics; 2006, http://dx.doi.org/10.2514/4.866821.
[27] Vieira R, Virtuoso F, Pereira E. A higher order model for thin-walled structures with deformable cross-sections. Int J Solids Struct 2014;51(3–4):575–98. http://dx.doi.org/10.1016/j.ijsolstr.2013.10.023.
[28] Genoese A, Genoese A, Bilotta A, Garcea G. A generalized model for heterogeneous and anisotropic beams including section distortions. Thin-Walled Struct 2014;74:85–103. http://dx.doi.org/10.1016/j.tws.2013.09.019.
[29] Dikaros IC, Sapountzakis EJ. Distortional analysis of beams of arbitrary cross section using bem. J Eng Mech 2017;143(10). http://dx.doi.org/10.1061/(asce)em.1943-7889.0001340.